The effect of tail geometry on the slipstream and unsteady wake structure of high-speed trains

J.R. Bell [a],*, D. Burton [a], M.C. Thompson [a], A.H. Herbst [b], J. Sheridan [a]

[a] Department of Mechanical and Aerospace Engineering, Monash University, Clayton, Victoria 3800, Australia
[b] Centre of Competence for Aero- and Thermodynamics, Bombardier Transportation, Vasteras, Sweden

ARTICLE INFO

ABSTRACT

The effect of varying the roof-angle of the tail of a generic high-speed train on the unsteady wake structure and corresponding slipstream is investigated in a 1/10th scale wind-tunnel experiment. Insight into the slipstream and unsteady flow features are gained from 4-hole dynamic pressure probe measurements, surface-flow visualisations, measurements from a two-dimensional array of total pressure probes, and frequency analysis. The results show that increasing tail roof angle leads to a transition from an unsteady wake with a pair of streamwise vortices that exhibit sinusoidal, antisymmetric motion to an unsteady wake dominated by large-scale separation with vortex shedding from the sides of the train. It is the interaction of the streamwise vortices with vortex shedding from the sides that results in the widest unsteady wake, and consequently, the largest slipstream velocities.

1. Introduction

The wake of a HST is where the largest *slipstream* velocities are found to occur [1–4]. Slipstream is the air flow induced by a vehicle's movement. In practice, it is measured at a fixed distance from the vertical centreplane of the train. It is an important consideration for the aerodynamic performance but also for the safe operation of high-speed trains (HSTs). Such flows can be hazardous to commuters waiting at platforms and to track-side workers [5] due to the significant pressure forces. Regulations are in place that limit the magnitude of slipstream velocities a HST can induce [6,7].

The importance of streamwise vortices to the wake structure of a HST has been identified in literature [1,8,9]. In particular, the authors have associated the high slipstream velocities in the wake to the presence of a time-averaged streamwise vortex pair [3,10]. As the vortices move downwards and outwards beyond the passage of the train, the largest slipstream velocities are measured.

In the time-varying wake, the authors have identified signs of periodic spanwise oscillations of the vortex pair, caused by merging and interaction of von Karman-like vortex shedding from the train side surfaces [10,11], as illustrated in Fig. 1. This time-varying nature of the flow is the proposed cause of peak instantaneous slipstream velocity, which has been found to vary

in magnitude and location in the wake both experimentally [1,4] and numerically [12–14].

The overall shape of a HST is determined by its numerous aerodynamic characteristics, the necessity of bi-directional operation and aesthetic design. In general, a longer nose HST with large roof slant and small side taper has a minimum head pressure pulse travelling in open air [15]. The lengthwise rate of change in cross-sectional area of the nose can be optimised to reduce the micro pressure pulse that builds up when a HST enters a tunnel and has the potential to cause shock-waves at tunnel exits [15].

During exposure to crosswinds, the nose and leading cars of a HST experience the greatest over-turning moments. As a result, the curvature of the nose geometry and roof edge geometry greatly influences the uneven pressure distribution resulting from crosswind and thus can be optimised to improve crosswind stability [16]. The nose of the HST has minimal separation, as the geometry is typically optimised to reduce its pressure pulse, thus its contribution to the vehicle's overall drag is limited [15]. The high L/H of a HST results in the body surface (skin friction $\approx$35% of total drag) and underbody roughness ($\approx$44% of total drag) being the primary sources of aerodynamic resistance [15], both being dependant on the length of the vehicle. The tail geometry of the vehicle, the same as the nose geometry, and the resulting wake structure are important for pressure drag and are also proposed to be important for slipstream.

The sensitivity of the wake structure of a HST to its tail geometry has been established by a number of investigations.
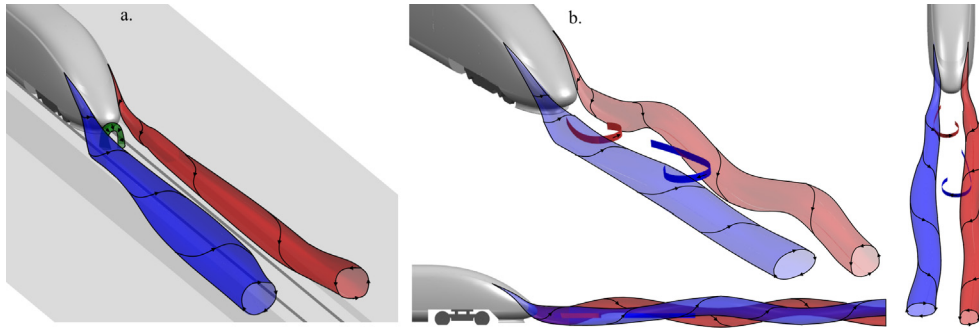

Fig. 1. (a) Time-averaged wake topology, (b) unsteady wake topology: a pair of oscillating longitudinal vortices and Karman-like vortex shedding in the horizontal plane. (First appeared in [10,11], respectively.)

Experimental work by Morel [17] on a fundamental shape similar to that of a HST—a square cylinder with a base slant—indicated the wake of such a body is dominated by separation and/or a pair of streamwise vortices. These findings are similar to those of Ahmed [18–20] for a model automotive body geometry. Scaled wind-tunnel experiments of two realistic HST geometries by Weise et al. [8] confirmed such a result. Surface flow visualisation on the tunnel floor and smoke flow visualisations showed the vortex regime exhibited a wider wake. Muld et al. [12] also numerically investigated two HST geometries and found the *ICE2* exhibited a coherent pair of streamwise vortices, in comparison to a *CRH1* HST where separation at the tail dominated the wake topology.

Although literature has clearly shown the tail geometry can affect the wake structure, a desired wake topology for optimal slipstream performance, i.e., low slipstream velocities in the near-wake, has not been found. Full-scale experiments on a variety of operational HSTs by Baker et al. [2] have suggested that in general, HSTs with more 'rounded' tails (*ICE3* and *S100*) exhibited a more gradual rise to the near-wake slipstream peak compared to those with less rounded tails (*S120, S130, ICE1/2*), which exhibited a sharper rise. A larger magnitude accompanies the steeper rise, as observed by Baker et al. [2], and in general corresponds to a larger peak value from gust analysis.

Considering the range of geometric parameters in operational HSTs, it is clear that there is considerable scope to optimise a HST's geometry for slipstream performance. Previous work has found that a HST with a sufficiently sharp roof slant angle will form streamwise vortices, and it is proposed that other parameters such as side taper and corner angle will also affect these dominant wake structures, either in strength, coherence or location. No existing literature has explicitly established the link between HST tail geometry, the resulting unsteady wake structure and the corresponding slipstream.

In this work, the slipstream, and the time-averaged and unsteady wake structure, of 7 different tail geometries based on the Inter-City-Express 3 (ICE3) HST geometry, is presented. The ICE3 HST is a high-speed train that operates throughout Europe and Asia, and the geometry is freely available [21]. A sequence of increasing roof angles was chosen to progressively transition from a wake topology dominated by the pair of counter-rotating streamwise vortices at low roof angles to full separation at high roof angles. This was intended to explore and characterise the association of the near-wake peak in slipstream with the presence of the streamwise vortices. In addition, the changing wake topology resulting from the changing geometry enables greater insight into the flow components constituting the entire 3D steady and unsteady wake structure. This work, part of a collaboration between Monash University and Bombardier Transportation, contributes to the understanding of the effect train geometry has on the wake structure and consequent slipstream. Ultimately, it is

hoped that the insights presented will contribute to the design optimisation of the future generation of HSTs.

2. Methodology

2.1. Experimental model

The geometry of a Deutsche Bahn Inter-City-Express 3 (ICE3) high-speed train is the basis for the tail models investigated. The external shape, and thus external aerodynamics, are the same as the Siemens Velaro HST. This HST is in operation throughout Germany, Netherlands, Belgium, Austria, Switzerland, Denmark, France, Spain, Turkey, Russia, and China. The HST Computer-Aided Design (CAD) model geometry is freely available from the TC 256 Secretariat held by the DIN Standards Railway Committee (FSF) [21]. The availability of the ICE3 geometry, its wide use throughout the world, and its modern aerodynamic shape that is similar to other current HSTs in operation makes it an ideal geometry for investigating high-speed train aerodynamics.

A ICE3 1/10th-scale wind-tunnel model was the baseline for the experiment. It measured $5.0 \times 0.3 \times 0.4$ m^3 ($L \times W \times H$), with a cross sectional area of ≈ 0.12 m^2. The model had four sets of bogies, no pantographs, no inter-carriage gaps and no heating, ventilation and air conditioning (HVAC), as the essential geometry—the gross external shape—is the focus of this investigation. The model was supported by 6 pairs of $0.05H$ (20 mm) diameter cylindrical supports in line with the wheels in the bogies.

A simplified HST tail geometry was developed to assess the sensitivity of the wake structure and slipstream to tail geometry. The geometry started from the same cross-sectional profile of the ICE3 wind-tunnel model, while the roof angle varied from 20 to 90° from the horizontal plane (see Figs. 2 and 3). The model was predominantly 2D, with the roof corner and nose corner fitting to a 150 mm diameter ($0.375H$), with 50 mm ($0.125H$) diameter rounding on the side edges. Due to the reduced tail length of the geometries with sharp roof slant angles, the rear-most bogie that is present in the ICE3 model is not included in the simplified tail geometries.

2.2. Experimental setup

A train travelling on a straight track over flat ground with no crosswind was modelled in the experimental setup. This approach aims to isolate the wake and resulting slipstream characteristics generated by the essential generic train geometry in an ideal environment. The experiment was performed in the Monash University 1.4 MW closed-circuit wind tunnel (Fig. 4). Fixed-pitch axial fans are driven by a 1.4 MW quad-motor system capable of achieving speeds between 5 and 65 m/s.
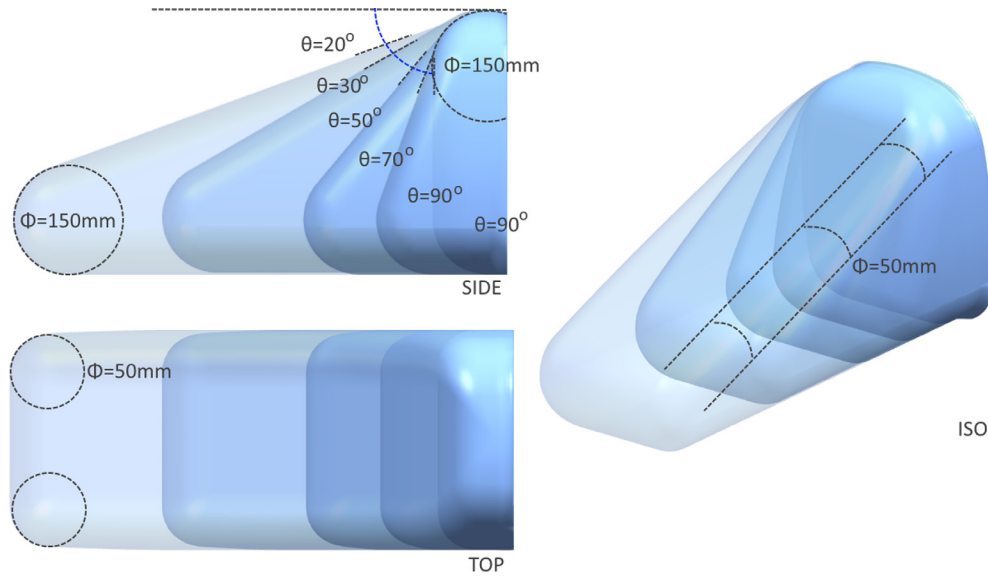
Fig. 2. Fundamental HST geometry, predominantly 2D in overall shape. Roof and nose diameter = 150 mm ($0.375H$) with all other edges having diameter = 50 mm ($0.125H$) rounding. Roof slant angles tested were $20, 30, 50, 70, 90°$ Rd (with rounded edges), and $90°$ Sh (with sharp edges, no rounding).
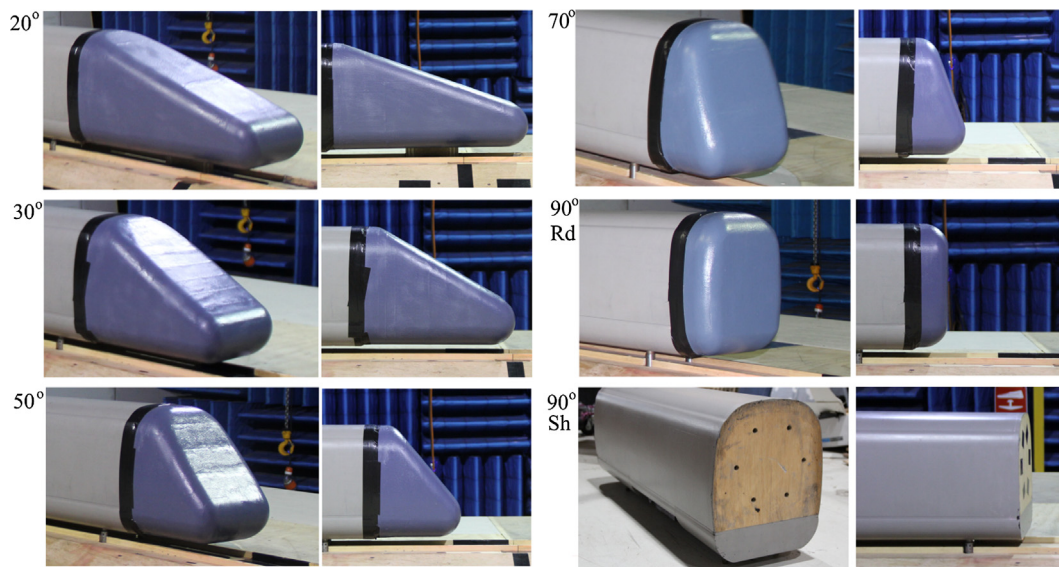

Fig. 3. Fundamental HST geometries: $20, 30, 50, 70, 90°$, and $90°$ with no rounded edges.

The experimental setup and the coordinate system adopted are presented in Fig. 5. Streamwise position, x, is normalised by the model height (H), with $x = 0$ corresponding to the position of the tail, as is the practice in general ground-vehicle aerodynamics [22,23] with a focus on the wake. In addition, literature has indicated that the near wake is dominated by the tail geometry [17,12]. Cross-stream position, y, is normalised by the model width (W), with $y = -1/2$ corresponding to the left vertical edge and $y = 1/2$ to the right edge. Vertical position, z, is normalised by model height, with $z = 0$ corresponding to the top of the rails (TOR).

The 3/4 open test section measuring $12 \times 4 \times 2.5 \text{ m}^3$ ($L \times W \times H$) was fitted with a 0.6 m ($1.2H$) high splitter plane to reduce ground boundary layer effects, resulting in a cross-sectional area above the splitter plane of 8.0 m^2. A 1/10th-scale *Single Track Ballast and Rail* (STBR) ground configuration (see Fig. 5b) was included in the setup, with height of 100 mm ($0.24H$), and upper and lower widths of 300 mm ($1W$) and 555 mm ($1.85W$), respectively, adhering to the EN [7]. The leading edge of the STBR had an front angle equivalent to the side angle ($37°$) swept 180 degrees. Velocity measurements established no separation occurred over the leading edge of the STBR. The maximum blockage ratio was $\approx 2\%$ above the splitter plate, including blockage due to the traverse and STBR. Thus, blockage effects are expected to be minimal, and no blockage corrections were applied. The approximate turbulence intensity (I_{uvw}) above the wind tunnel boundary layer was 1.6%, consistent with similar wind-tunnel experiments [16,20,24].

Results presented are from experiments performed at a Reynolds number, using width as the characteristic length, of $Re_W = 0.7 \times 10^6$, corresponding to a freestream velocity of $u_\infty = 35 \text{ m/s}$. Sensitivity of the results to Reynolds number over the range $Re_W = 0.5 \times 10^6 - -1 \times 10^6$, corresponding to freestream velocities of 25–48 m/s, was tested and found to be
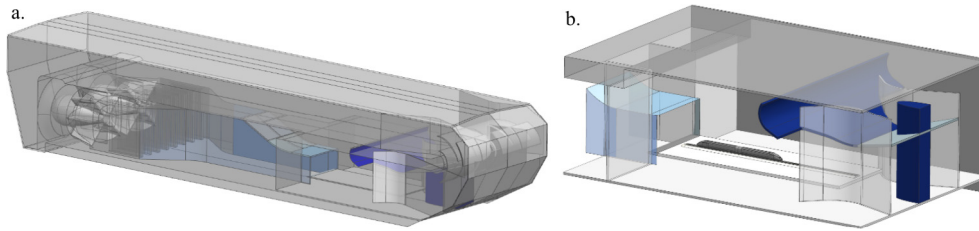
Fig. 4. (a) The Monash University 1.4 MW closed-return wind tunnel. (b) 1:10th-scale ICE3 model in the 3/4 open-jet test section. A 600 mm high splitter plate (shown) was utilised to reduce the ground boundary layer.
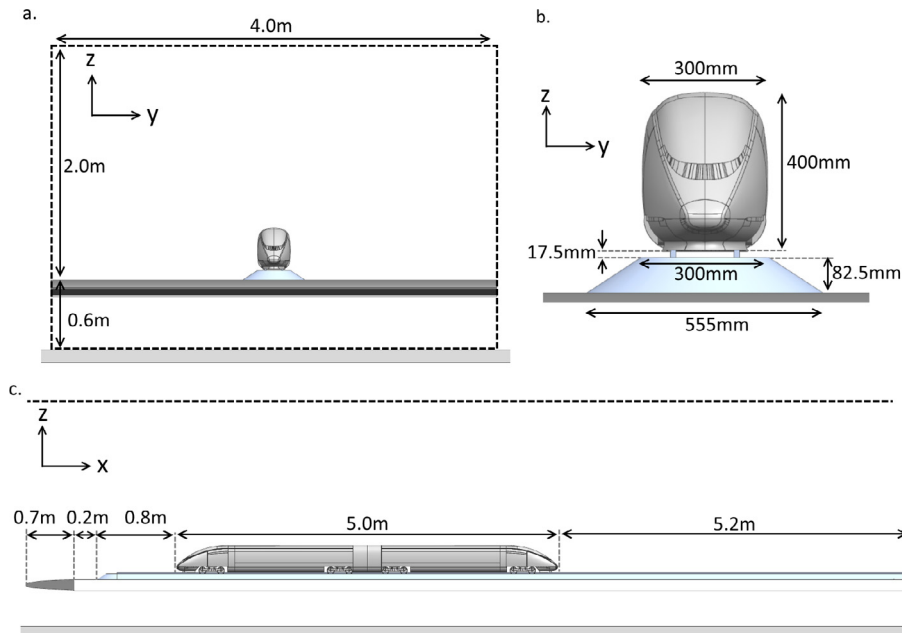

Fig. 5. The 1:10th-scale ICE3 model in the 3/4 open-jet test section of the Monash University 1.4 MW wind tunnel. A 600 mm high splitter plate was utilised to reduce the ground boundary layer.

negligible, however this is still significantly smaller than the typical full-scale Reynolds number of 17×10^6 (corresponding to a full-scale train travelling at 300 km/h).

The measured displacement thickness of the boundary layer was δ^*/H = 0.006 and 0.035 at the model's nose and tail positions, respectively, in an empty tunnel above the splitter plate. The presence of the ground boundary layer is an experimental limitation, due to the incorrect relative motion between the model and the ground. In wind tunnel experiments, this may be overcome by utilizing a moving ground, which is a costly solution and particularly difficult to apply with long HST experimental models [25] and with the ballast modelled. The stationary ground is expected to result in a flatter wake structure as the trailing vortices move away from the model and approach the ground [26–28]. This may affect the magnitude and location of the near-wake peak in slipstream velocity to an extent. However, a number of researchers have found the formation of trailing vortices of interest in this study are largely insensitive to the presence of a stationary/moving ground [23,29]. Further discussion on these effects have been presented in Bell et al. [10]. As the focus in this study are the existence of trailing vortices and large-scale separation from the roof, the ground boundary layer is proposed not to have a significant influence on the overall findings.

The side and roof boundary layers were measured and analysed as 2D boundary layers for simplicity, as previous researchers have done [1,30]. The displacement thicknesses of the boundary layer at

$x = -2.5, z = 0.5$, at the side, $x = -2.5, y = 0$ on the roof, were $\delta^*/H = 3.12 \times 10^{-2}$ and 2.82×10^{-3}, corresponding to momentum thicknesses of $\theta/H = 2.50 \times 10^{-2}$ and 2.70×10^{-3}, respectively.

The boundary is slightly thinner than the range of boundary layer thicknesses ($\delta^*/H = 5 \times 10^{-2} - 1 \times 10^{-1}$) measured on full-scale HSTs by Sterling et al. [31]. The reduced length of $L/H = 14$ of the model is the likely cause, as full-scale HSTs operate in the range of $L/H = 25$ or above. The authors have investigated the sensitivity of the slipstream and wake structure of the same ICE3 HST model in the same experimental setup over the range of lengths $L/H = 6 - 14+$, where greater than $L/H = 14$ was achieved with boundary layer augmentation. The results showed that even with a significant range of boundary layer thicknesses at the tail ($\delta^*/H = 1.4 \times 10^{-3} - 6.3 \times 10^{-2}$), the salient time-average and unsteady features of the wake, and corresponding slipstream were consistent [32]. Thus, the findings of this experiment are proposed to translate to a HST with a typical L/H.

2.3. 4-Hole dynamic pressure probe

Measurements were taken with a 4-hole dynamic-pressure probe (cobra probe). Specifications indicate that the cobra probe is capable of determining velocities with the accuracy of ± 1 m/s within a $\pm 45°$ cone angle; however, it is not capable of measuring reversed flow [33]. Despite this, an indication of the percentage of

flow that is outside its calibrated cone of acceptance is provided by the probe's accompanying analysis software, and in all cases reported >95% of measurements were within the cone of acceptance.

To obtain slipstream profiles, two cobra probes were mounted with $0.25H$ (100 mm) spacing and were moved using a computer-controlled mechanical traverse. Streamwise (x direction) sweeps with a high spatial resolution $0.05H$ (20 mm), were performed at $x = -15H$ (upstream of the nose) to $10H$ (in the wake), at $y = 2(W/2), z = 0.05 \& 0.3H$ above the top of rail (TOR). These chosen positions are representative of the locations where people or infrastructure might be influenced by the induced flow around the vehicle. The lower measurement height directly corresponds to the positions at which a HST is assessed for slipstream homologation in European regulations [6,7].

Measurements for flow mapping were taken in spanwise (yz) planes at $x = 1$ and $6H$, on a square grid of $\Delta y, \Delta z \approx 0.05$. Measurements were performed in both the positive and negative y domain to confirm centreplane reflection symmetry of the flow, with only a half-plane presented. Two cobra probes mounted with $0.25H$ (100 mm) spacing were positioned using an automated traverse. These measurements had a sample time of 15 s and a sampling frequency of $f_s = 1000$ Hz.

The velocities measured by the cobra probe in the wind tunnel have a train-fixed (TF) frame-of-reference. The component of the velocity in the x direction (u) was converted to the ground-fixed

(GF) frame-of-reference, the perspective of a stationary observer who experiences slipstream, and normalised against the free-stream velocity:

$$u_{GF} = 1 - \frac{u_{TF}}{u_\infty}. \tag{1}$$

The reference velocity, u_∞, was calculated from an upstream reference pitot-static tube, corrected to the model's position through a dynamic-pressure correction factor.

The cobra probe, consisting of the set of tubes and four differential pressure transducers, is specified by the manufacturer (TFI) to have a frequency response above 2000 Hz.

2.4. Total-pressure array

A two-dimensional array in the yz plane of 120 total pressure probes, simultaneously measured, was used to measure the unsteadiness of the wake. The probes had a spatial resolution of $0.05H(0.125(W/2))$. Each probe was connected by 1.5 m of tubing to a 128 channel Dynamic Pressure Measurement System (DPMS). The phase and amplitude of the pressure measured were corrected using the *inverse transfer function* (ITF) method [34]. The frequency response of the pressure measurement system was determined theoretically using the method outlined by Bergh and Tijdeman [35]. This method of correction is common in similar dynamic-pressure measurements in applied aerodynamics research such
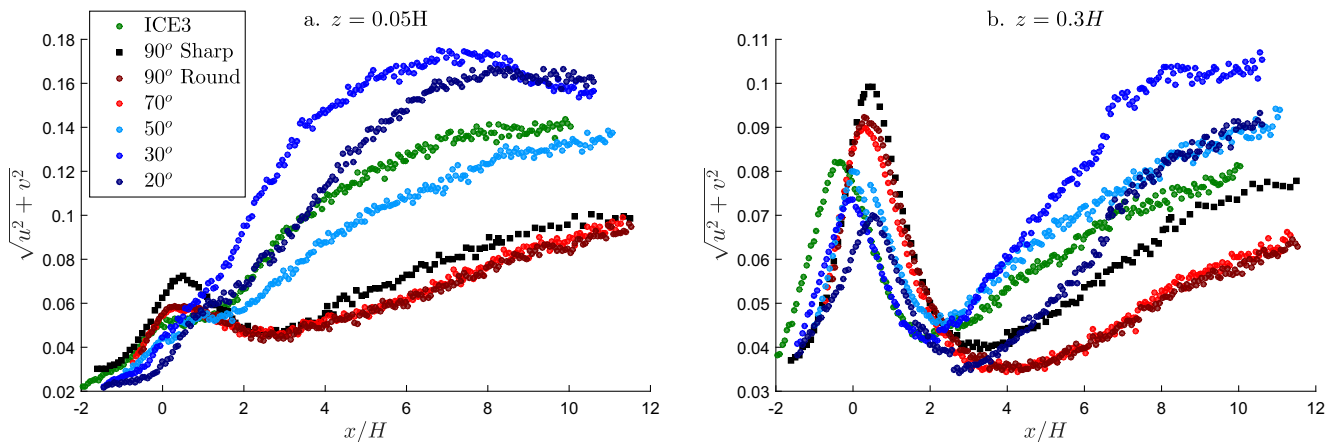

Fig. 6. Mean slipstream velocity, $\sqrt{u^2 + v^2}$, for the different geometries tested at (a) $z = 0.05H$, and (b) $z = 0.30H$.
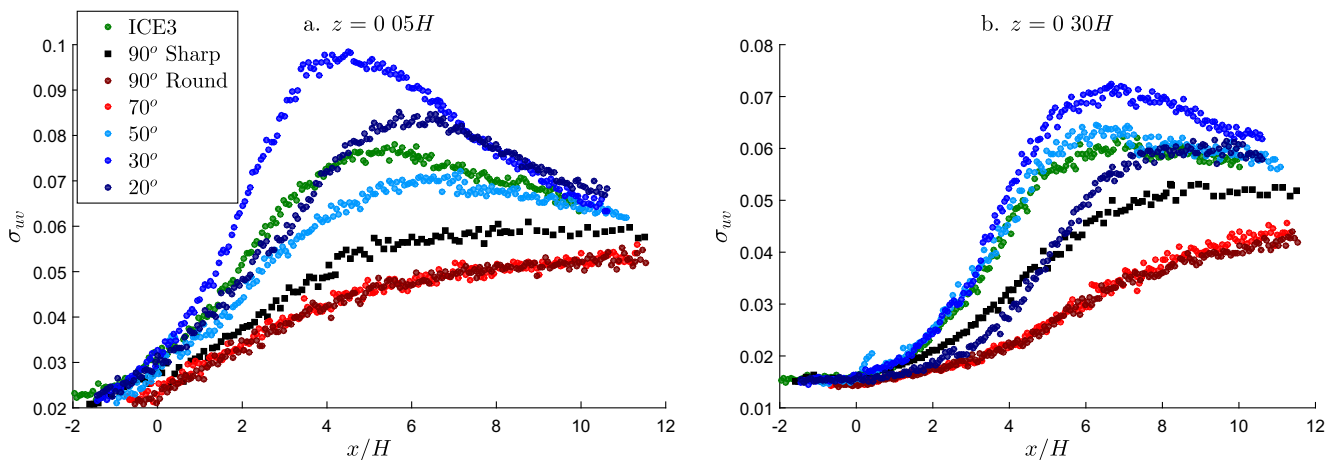

Fig. 7. Standard deviation of slipstream velocity, σ_{uv}, for the different geometries tested at (a) $z = 0.05H$ and (b) $z = 0.30H$.
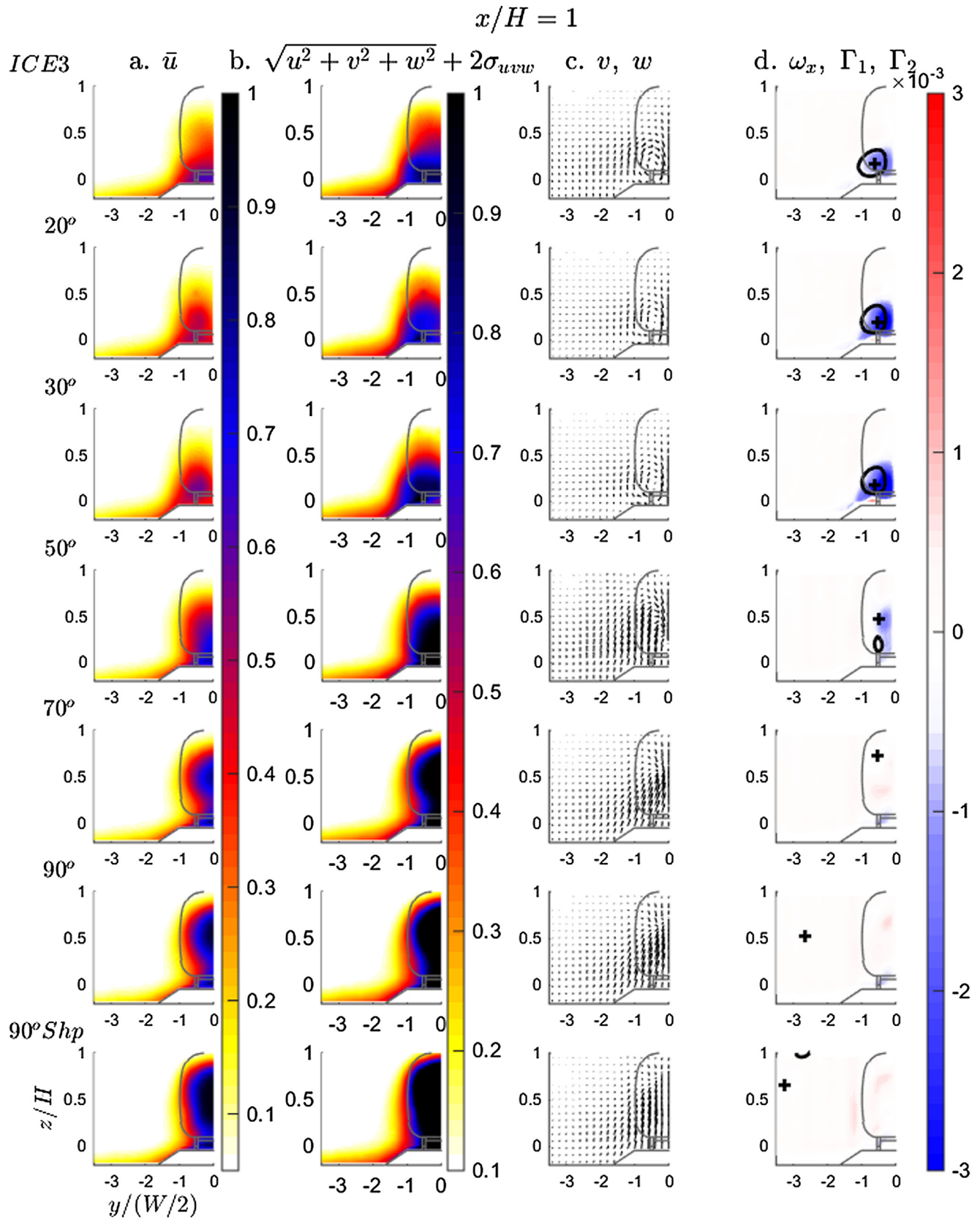
Fig. 8. Time-averaged wake topology in the yz plane at $x = 1H$. (a) $\overline{u}$, (b) $\overline{U} + 2\sigma_{uvw}$, (c) $\overline{v}, \overline{w}$ vectors, (d) Streamwise vorticity colormap of ω_x, Contour lines of $\Gamma_2 = 2/\pi$, with + indicating the position of max[Γ_1]. (For interpretation of the references to color in this figure legend, the reader is referred to the web version of this article.)

Fig. 9. Time-averaged wake topology in the yz plane at $x = 6H$. (a) $\bar{u}$, (b) $\overline{U} + 2\sigma_{uvw}$, (c) $\overline{v}, \overline{w}$ vectors, (d) Streamwise vorticity colormap of ω_x, contour lines of $\Gamma_2 = 2/\pi$, with + indicating the position of max[Γ_1]. (For interpretation of the references to color in this figure legend, the reader is referred to the web version of this article.)
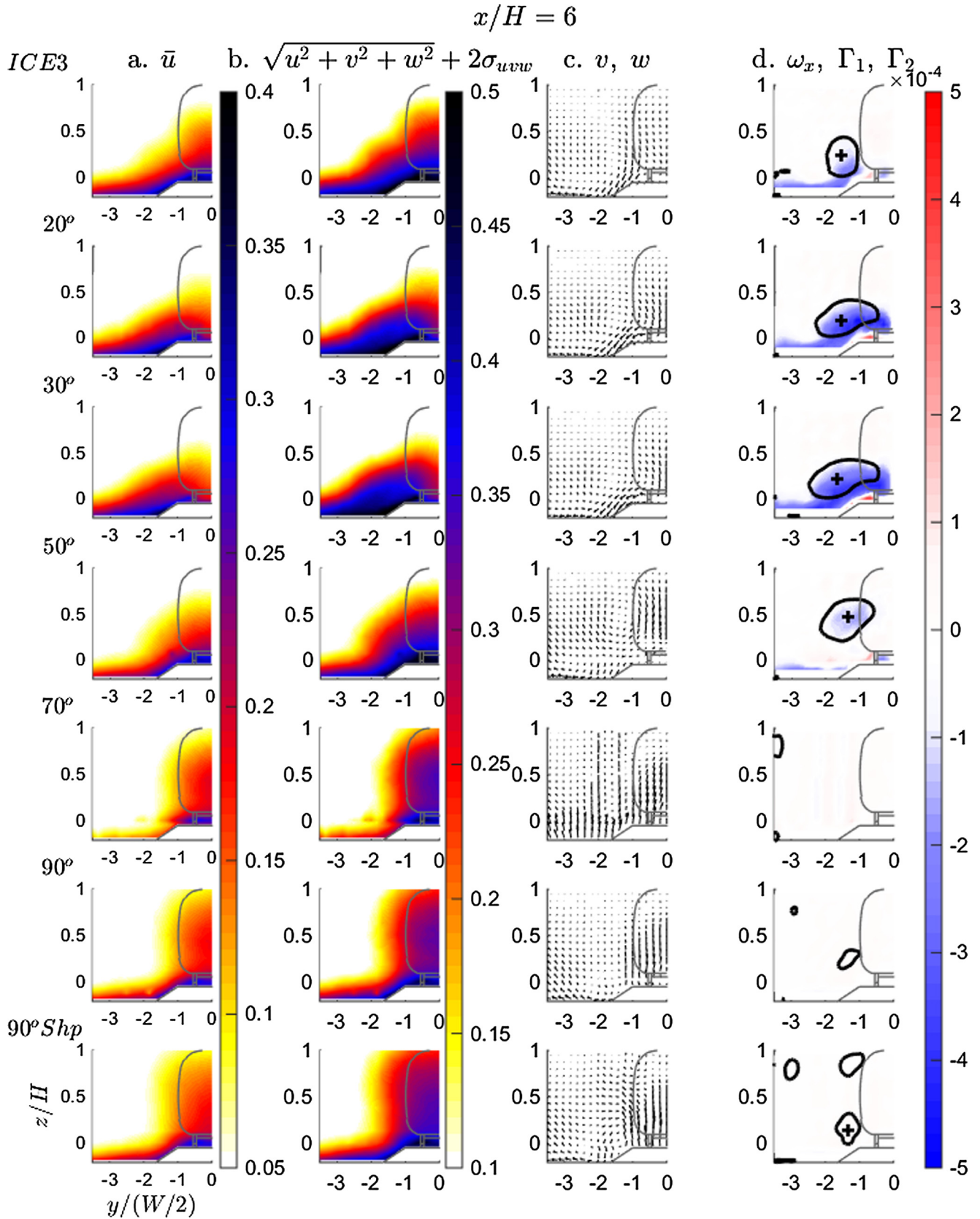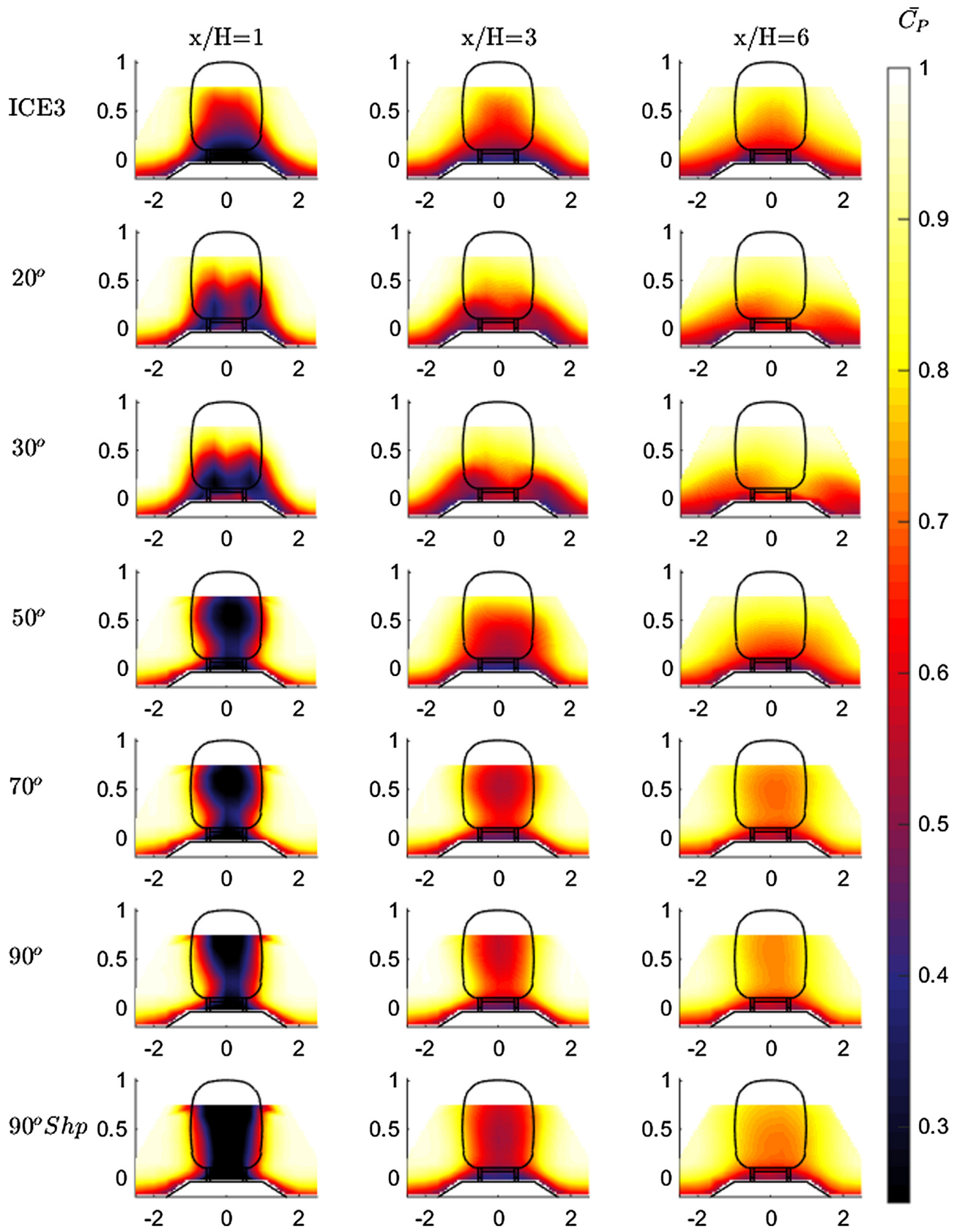
Fig. 10. Time-averaged total pressure, $\overline{C_P}$ measured by the TPA in the yz plane at $x = 1, \ 3, \ 6H$ for the 7 different tail geometries.

as [20,36]. Irwin et al. [34] has shown through experiments that the ITF method reduces the average magnitude of error—defined as the average percentage difference of pressure at each discrete time-step—between the true and measured pressure from 9.6% and 27.4% to 1.6% and 4.1% for tubing systems of 0.6 m and 3 m respectively, covering the tube length utilised in this experiment.

Two characteristic frequencies of the uncorrected frequency response are the frequency of the primary peak in the amplitude response, and the frequency where the amplitude response falls below 0.4. The frequencies where the primary peak in amplitude occurred were $St_W = 0.36$ (42 Hz). The amplitude response fell below 0.4 at $St_W = 6.9$ (810 Hz). The dominant frequencies of the baseline ICE3 model have previously been published at $St_W \approx 0.2$ [10], corresponding to frequencies in the range of 20–30 Hz in the scaled wind-tunnel experiment. Thus, the frequency response of the pressure measurement systems is suitable for the range of frequencies of interest.

The sampling frequency was limited to $f_s = 1000$ Hz to prevent overloading the data acquisition system due to high bandwidth from multiple simultaneous measurements. This sampling rate in the 1/10th-scale experiments with freestream velocities of 25–45 m/s corresponds to 333–185 Hz for a full-scale, operational HST travelling at 300 km/h. Measurements had sampling times of 60 s.

True total pressure of the flow is not measured as the probes are forward facing and measuring in a region where the flow exhibits some degree of pitch and yaw. It is the summation of the dynamic pressure associated to the streamwise direction due to the u component of velocity, and the static pressure. This pressure, P_i, was converted to the coefficient of pressure using total, P_t, and static pressure, P_s from an upstream reference pitot-static tube:

$$C_P = \frac{P_i - P_s}{P_t - P_s}. \tag{2}$$

Calibration of the total pressure array (TPA) in an unobstructed test section being yawed up to $\pm 45°$, found that for up to a $\pm 15°$ angle the cosine relationship of total pressure derived from the u component was consistent. Thus, where the flow exhibits pitch or yaw of above $\pm 15°$ degrees, the measurements are only a proportion of the dynamic pressure associated with the streamwise direction and static pressure.

The TPA is an additional source of blockage in the wake of the model, at 1.2% of the jet cross-sectional area. Surface pressure measurements on one half of the tail, published in [10], were performed with the x position of TPA varied from $x = 1$ to $6H$ from the tail was performed. Results showed the overall pressure distribution shape did not change, however there was an average increase in pressure across the 120 taps with decreasing x position of the TPA. At $x = 1H$, the average increase in the coefficient of pressure was 0.04, which is less than 10% of the range of pressures recorded over the tail surface.

3. Results

3.1. Slipstream

Streamwise profiles of slipstream velocity in the wake are presented in this section. The slipstream in the wake is the focus here, as previous work by the authors has established it is the location of peak velocity, due to the presence of a pair of vortices moving behind the path of the train [3,10]. The mean slipstream profiles measured at $z = 0.05H$ and $z = 0.30H$ for the 7 geometries are presented in Fig. 6. The resultant velocity of the u and v components of velocity, $\sqrt{u^2 + v^2}$ is presented, as velocity in the horizontal plane presents the safety risk for destabilisation, in contrast to the vertical w component [6,7].
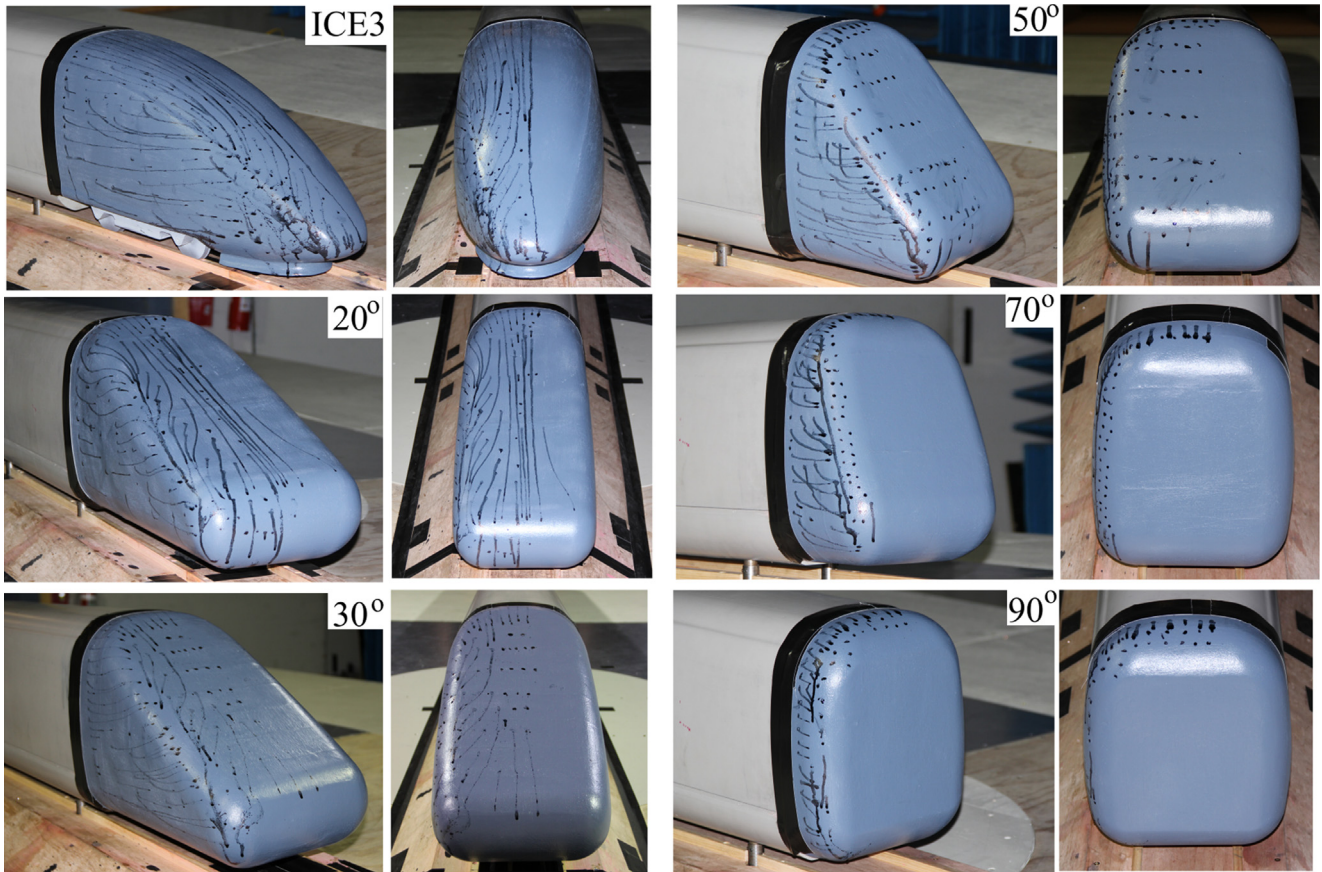

Fig. 11. Surface flow visualisations over each of the different tail geometries using ink drops to highlight the surface skin-friction patterns.
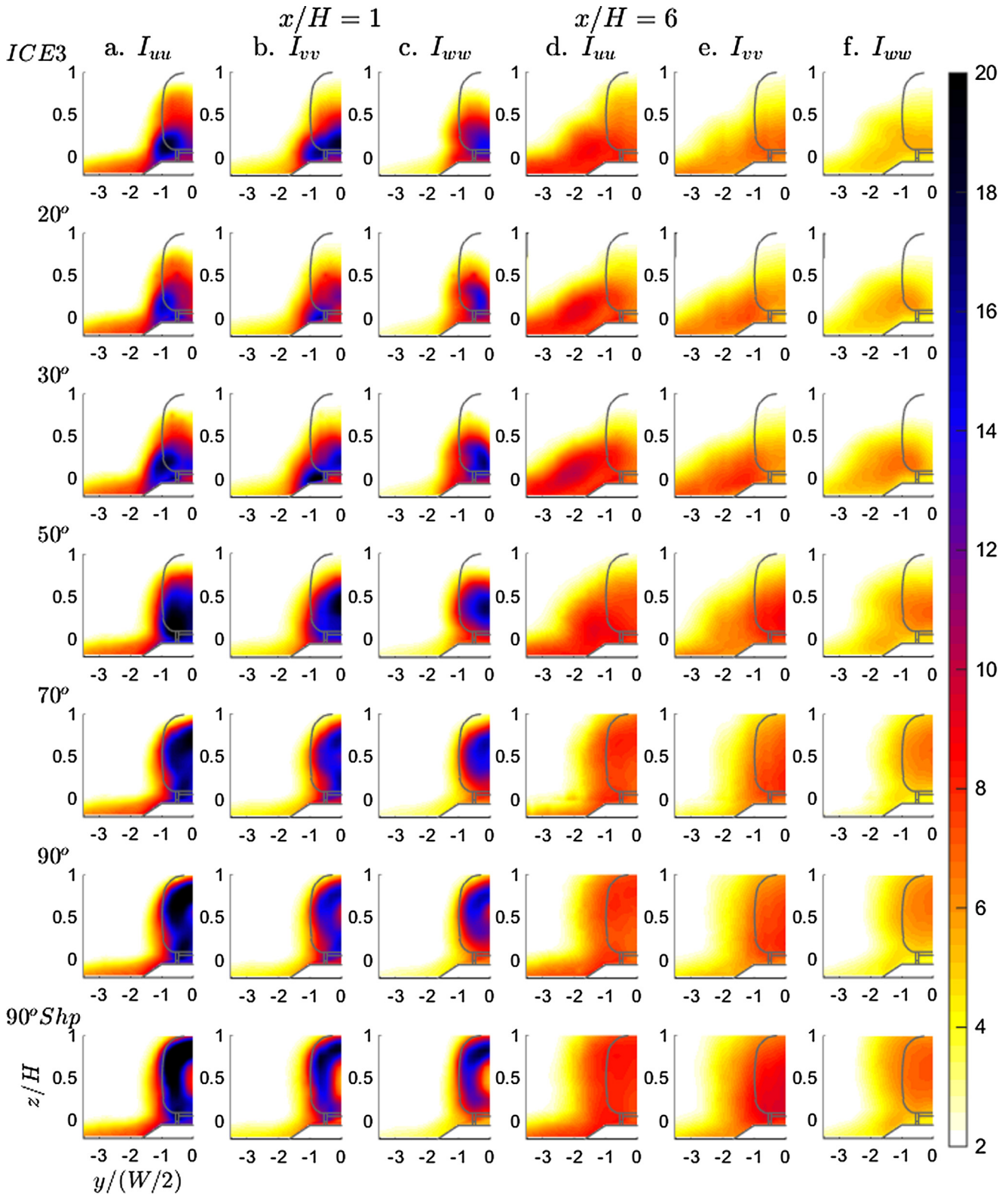
Fig. 12. Turbulence intensity in the streamwise, I_{uu}, spanwise, I_{vv}, and vertical directions I_{ww}, measured in the yz plane by cobra probes at $x = 1H$ and $x = 6H$ for the 7 different tail geometries.

The geometries with large roof angles (70°, 90° round, and 90° sharp) have significantly reduced slipstream velocity for the entire wake at both measurement heights; the near-wake peak is ≈35% lower at $z = 0.05H$. The 90° sharp geometry does show a larger peak at the tail, likely due to coherent separation at the fixed

trailing edge. The 50° roof geometry has lower slipstream at $z = 0.05H$ and higher at $z = 0.30H$.

In contrast, the low roof-angle geometries of 20 and 30° exhibit significantly larger slipstream velocities at both measurement positions. Interestingly, the 20° geometry has lower slipstream
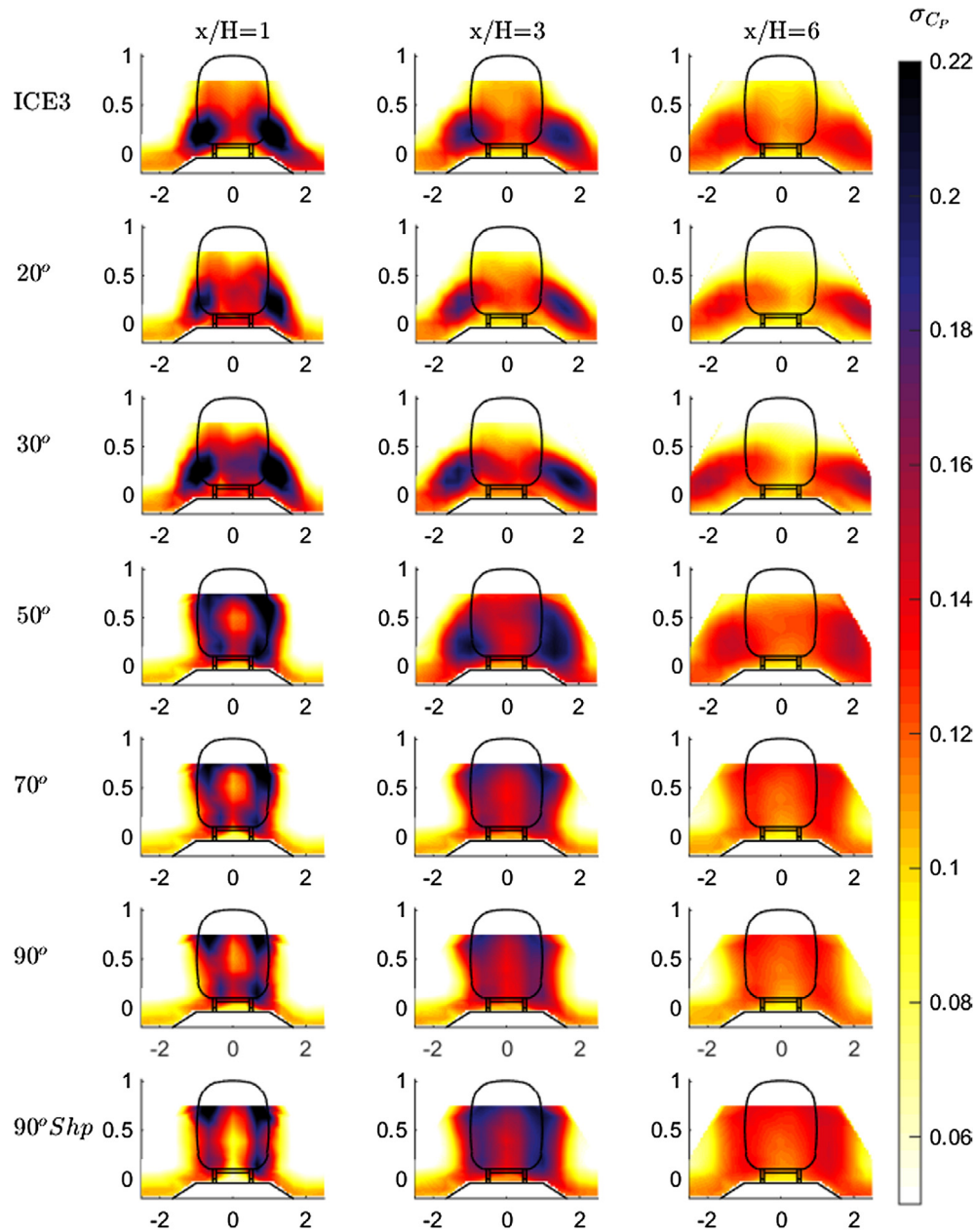
Fig. 13. Standard deviation of total pressure, σ_{C_P}, measured by the TPA in the yz plane at $x = 1, 3, 6H$ for the 7 different tail geometries.

velocity at both measurement heights than the 30° geometry, indicating there is a critical roof angle that leads to the largest slipstream velocities.

The standard deviation profiles in Fig. 7 show similar trends to the mean profiles. The 20 and 30° geometries exhibit significantly larger velocity fluctuations at the near-wake peak than seen for the ICE3 and the 50° cases, which are similar. The 70°, 90° round and 90° sharp cases have significantly lower fluctuations in slipstream velocity. These results show that the tail geometry has a significant impact on the slipstream of a HST.

3.2. Time-averaged wake

The time-averaged wakes of the 7 different tail roof geometries in the yz plane at $x = 1H$ and $x = 6H$ characterised by cobra-probe measurements are presented in Figs. 8 and 9. The induced streamwise (u) velocity field, a measure of the peak velocity,

$\sqrt{u^2 + v^2 + w^2} + 2\sigma_{uvw}$, vectors of v, w velocity, streamwise vorticity, ω_x, and vortex identifiers Γ_1 and $\Gamma_2 = 2/\pi$ are each presented.

These results clearly explain the cause of the high slipstream velocities for the geometries with low roof angles–the presence of a streamwise vortex. The ICE3, 20° and 30° geometries each have a distinct streamwise vortex (one of a pair) identified in the v, w velocity vectors, streamwise vorticity, ω_x, and the vortex identifiers Γ_1 and Γ_2. The 50° geometry shows a streamwise vortex that is much clearer at $x = 6H$ (Fig. 9).

In contrast, the geometries with larger roof angles have significantly larger slipstream velocities in their wakes (equal or exceeding the train speed) than the smaller roof angle geometries. However, these high slipstream velocities remain directly behind the vehicle, thus presenting significantly lower risk to safety and damage to infrastructure. Importantly, no coherent streamwise vortices exist in the wake for these larger roof-angle geometries.

These results are consistent with experimental and numerical work that established the sensitivity of the wake structure to the tail geometry, as well as the tendency of the wake to be dominated by trailing vortices or large-scale separation [17,12,8].

The mean total pressure in the yz plane at $x = 1$, 3 & $6H$, measured by the TPA (Fig. 10) provide a similar picture to the cobra probe flow mapping. The large roof angles experience significantly greater total pressure loss in the wake and presumably higher associated drag, yet this region remains directly behind the vehicle.

3.3. Surface flow-visualisation

Flow visualisation using ink droplets over the tail surface of each of the 7 tail geometries are presented in Fig. 11. The surface-flow patterns show the convergence of the downwash over the roof, and flow around the sides to form the streamwise vortices, for the ICE3, $20°$, and $30°$ geometries. In contrast, separation of the flow over the roof and sides is clearly visible for the $50°, 70°$ and $90°$ geometries, with the $90°$ sharp-edged geometry also exhibiting separation at the sharp edges. The $30°$ case exhibits a small region of separation over the tail in the centre-plane, however the flow reattaches and the wake still forms a streamwise vortex pair as shown in Section 3.2. Thus, in general, the primary difference between the slipstream results can be attributed to a wake being dominated by a pair of streamwise counter-rotating vortices, or, large-scale separation, as a result of tail geometry.

3.4. Streamwise wake dynamics

The distribution of turbulence intensity in the three directions in the yz plane at $x = 1H$ and $x = 6H$ are significantly different for the different geometries (Fig. 12).

Two broadly different turbulence distributions are visible for the vortex-pair-dominated wake and the separation-dominated wake. The vortex-pair-dominated wakes, as already examined for the ICE3 results previously presented, exhibit high streamwise turbulence intensity, I_{uu}, in the streamwise vortex core, with a horizontal band of high spanwise intensity, I_{vv}, and a region of high vertical intensity, I_{ww}, at the tail tip.

In contrast, the separation-dominated wakes exhibit higher magnitude turbulence intensity ($I_{uu,vv,ww} \approx 20\%$) within the shear layers from the sides and roof of the model. These regions of high turbulence are consistent for the turbulence intensity in each direction, and do not move outwards beyond the body, marking

a significant difference from the vortex-dominated wakes. Additionally, the separation-dominated wakes contain distinct differences in the magnitude of the turbulence intensity in each direction: the streamwise intensity is higher than the spanwise intensity, which is in turn higher than the vertical intensity.

The standard deviation of the total pressure obtained from the TPA (Fig. 13) presents similar results to the turbulence intensity distributions mapped by the cobra probes. Regions of peak standard deviation in total pressure, σ_{C_P}, are visible in the vortex cores that move outwards further into the wake for the ICE3, $20°, 30°$, and $50°$ geometries. However, for the $70°, 90°$ round and $90°$ sharp geometries, high standard deviation of total pressure occurs in the shear layers from the sides and roof of the model, but this doesn't extend significantly beyond the width of the model.

3.5. Spanwise wake dynamics

The measurements from the TPA also provide insight into the dynamics of the wake in the spanwise plane. Oscillations of pressure in the yt plane (analysing a single spanwise row of total pressure probe measurements over time) have been previously observed in TPA measurements in the wake of ICE3 [11]. These oscillations were directly associated to periodic shedding of vortices occurring from the train sides that merge and influence the dynamics of the streamwise vortex pair. The shedding vortices were identified through measurements made by an array of 17 4-hole probes. Results measured at $x = 1H, z = 0.2H$ from both the TPA and the 4-hole probe array are presented in Fig. 14 to demonstrate the insight that can be gained from the TPA results, which are presented below for the 7 different geometries.

Spanwise slices of total pressure filtered with a single-pole, Butterworth lowpass filter of $St_W < 0.7$, and measured at $z = 0.2H$ are presented in Fig. 15 for each tail geometry. The spanwise oscillations in transient pressure, C_P, (Fig. 15a), and alternating regions of positive and negative fluctuating pressure, C'_P, (Fig. 15b) are visible in all configurations, however significant differences exist.

The ICE3, $20°, 30°$ and $50°$ geometries have very wide regions showing strong oscillations of total pressure relative to the larger roof-angle geometries. For the $20°$ and $30°$ geometries in particular, two regions of low total pressure visibly oscillate. These results are explained by the vortex shedding off the sides of the ICE3 geometry interacting with the streamwise vortices as described in detail by the authors previously [11]. The interaction of these two wake fea-
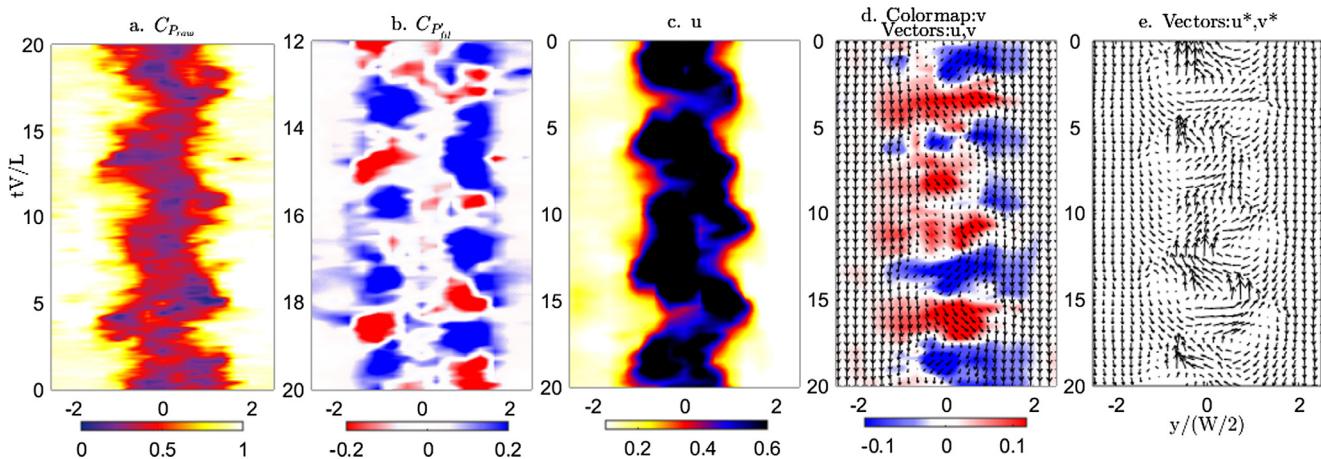

Fig. 14. (a) Transient C_P and (b) fluctuating total pressure, C'_P, measured by the TPA filtered with a single-pole, Butterworth lowpass filter of $St_W < 0.7$. (c) u velocity, (d) v colormap with u, v vectors overlaid and (e) u^*, v^* velocity vectors with a convection velocity of $0.6u_\infty$ downstream, measured by a spanwise array of 17 4-hole dynamic pressure probes. Both measurements obtained at $z = 0.2H, x = 1$. (For interpretation of the references to color in this figure legend, the reader is referred to the web version of this article.)
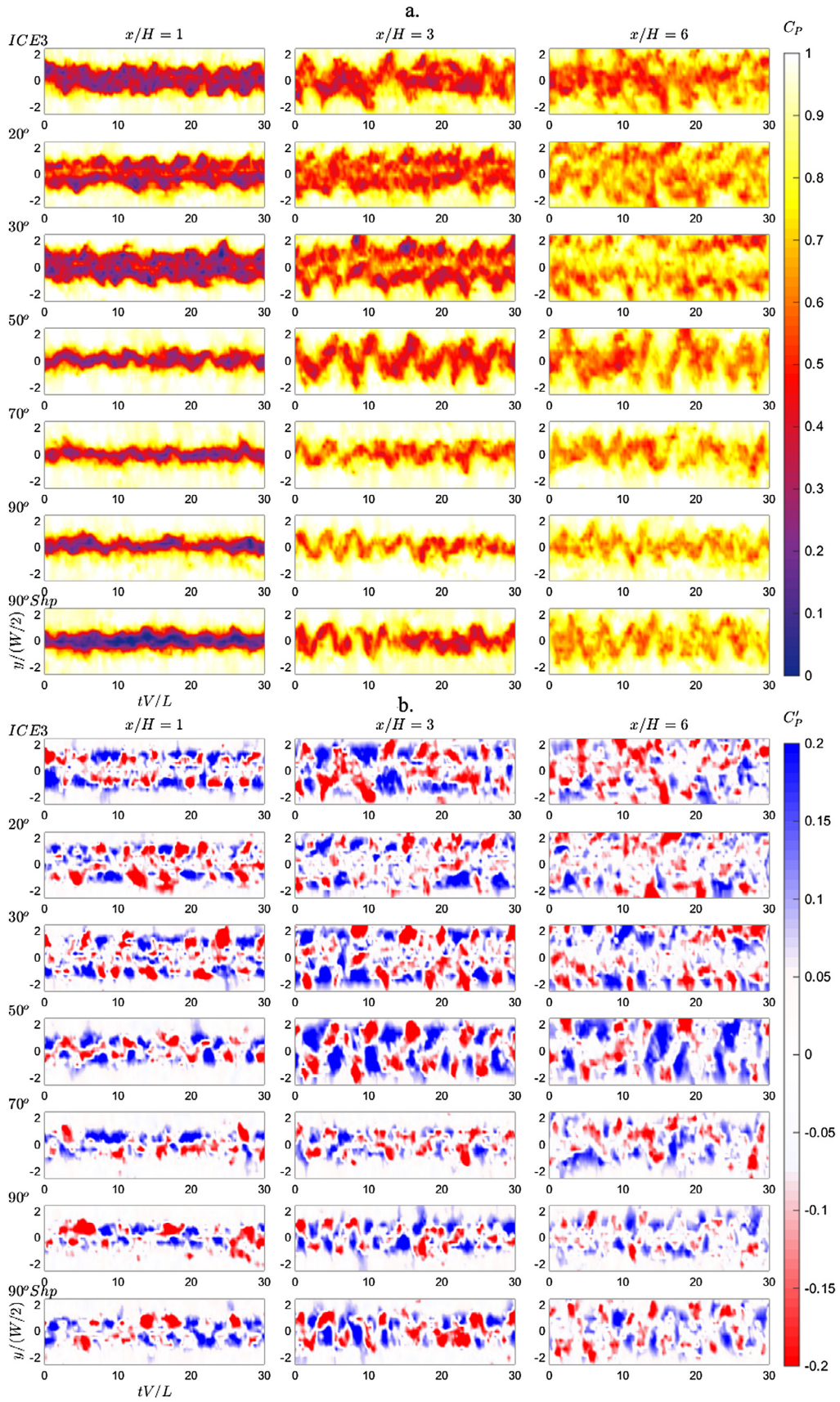
Fig. 15. (a) Transient C_P and (b) fluctuating total pressure, C_P' measured by the TPA at $z = 0.2H, x = 1, 3, 6H$ filtered with a single-pole, Butterworth lowpass filter of $St_W < 0.7$.
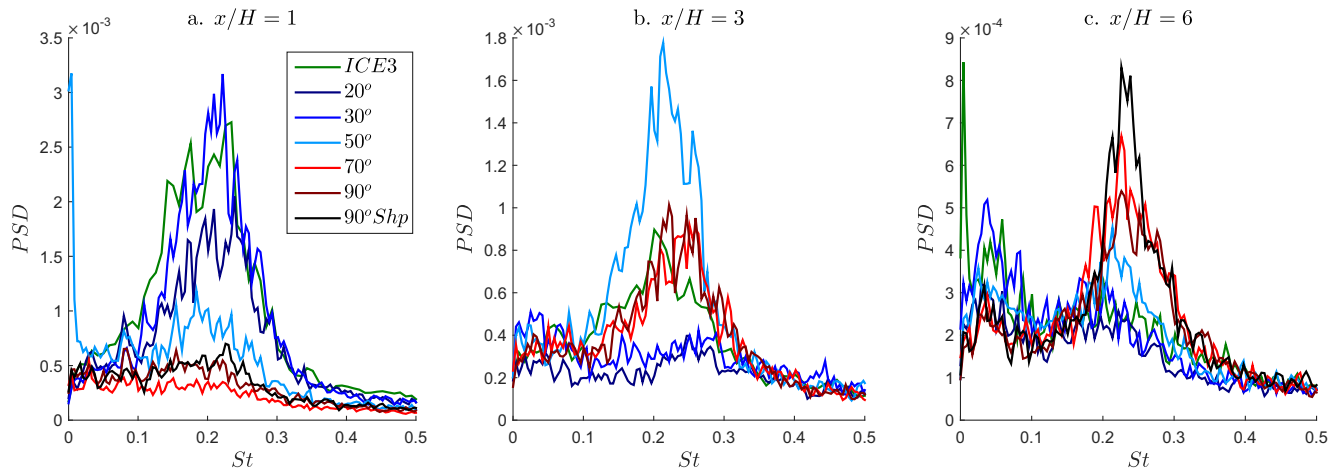
Fig. 16. Power spectral density of the total pressure measured by a probe in the TPA at $x = 1, \ 3, \ 6H, y = 1(W/2), z = 0.2H$ for different tail geometries.
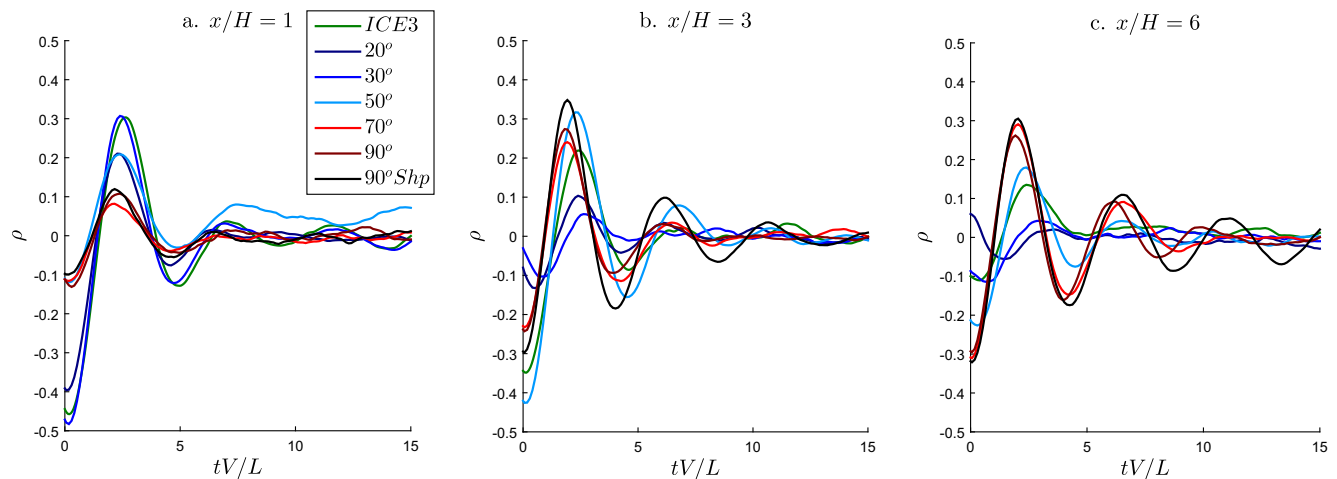

Fig. 17. Cross-correlation of the total pressure measured by two probes in the TPA at $x = 1, \ 3, \ 6H, y = \pm1(W/2), z = 0.2H$ for different tail geometries.

tures also result in a total pressure oscillation in the spanwise direction closer to the tail of the model.

For the large roof-angle geometries ($70°, 90°$ round, and $90°$ sharp) a weaker oscillation of the total pressure in the wake is also visible. Again, this is expected to be caused by vortex shedding occurring off the sides of the vehicle, however there are no streamwise vortices in the wake of these geometries to interact with. The total pressure in the wake does not oscillate as widely spatially as for the low roof-angle geometries, due to the absence of the streamwise vortices that move the wake outwards. The spanwise oscillation also takes longer to develop downstream for these large roof-angle geometries, with clear oscillations only occurring in the wake at $x = 3H$ and $x = 6H$, but not at $x = 1H$.

The identification of the dominant wake components explains the difference in slipstream results between the different tail geometries. The combination of both streamwise vortices interacting dynamically with vortex shedding off the sides creates a wider wake with peak slipstream velocities occurring due to cross-stream movement of the streamwise vortices. This type of wake occurred for the ICE3, $20°, 30°$ and $50°$ tail geometries, where flow over the roof remains attached over the tail surface yet has a strong induced down-wash from the low roof angle. This is presumably why the $30°$ geometry has a stronger oscillation and the worse slipstream, as the streamwise vortices are stronger compared with the $20°$ geometry.

Vortex shedding from the sides of the vehicle still occurs for tail geometries with large-scale separation ($70°, 90°$ round, and $90°$ sharp), however the resulting fluctuations in the wake do not reach far beyond the cross-stream extent of the vehicle. Thus, the slipstream profiles of geometries with large-scale separation are significantly lower.

3.6. Frequency and correlation

The power spectral densities (PSD) of the pressure measured at $x = 1H, y = 1(W/2), z = 0.2H$ for each tail geometry are presented in Fig. 16. The results show that the dominant frequency of $St_W \approx 0.2$ exists in the wake for all of these geometries. However, at the positions measured, the smaller roof-angle geometries exhibit a cleaner peak near to the tail, and a broader and weaker peak further downstream, while the large roof-angle geometries show the opposite, having much cleaner peaks further downstream into the wake.

Results from cross-correlation between two of the probes in the TPA at $x = 1H, y = \pm1(W/2), z = 0.2H$ (Fig. 17) reveal the phase relationship between the signals. Close to the tail at $x = 1H$, the low roof-angle geometries show strong evidence of the wake being $180°$ out-of-phase from side to side, through the negative correlation at zero time lag, and peak positive correlation at half the period ($tV/L = 2.5$) associated with $St_W = 0.2$. In contrast, the larger

roof-angle geometries show stronger signs of either side of the wake being 180° out-of-phase further into the wake at $x = 6H$.

4. Conclusions

The effects of the wake of seven different tail geometries were investigated in the scaled wind-tunnel experiment. These geometries were: ICE3, generic geometries based on the ICE3 but with roof angles of 20°, 30°, 50°, 70° and 90°, as well as a geometry with a 90° roof but with sharp trailing edges.

Slipstream measurements indicate that the lower roof-angles geometries (20°, 30°, 50°, ICE3) had higher slipstream at both measurement heights than the higher roof-angle geometries (70°, 90° round, and 90° sharp).

Surface flow visualisation of the geometries identified that these two groups were defined by whether or not large-scale separation occurred over the roof. Separation did occur for large roof angles, whilst the flow remained attached for small roof angles.

Flow mapping in the wake established that the geometries that exhibited large-scale separation did not produce a coherent pair of counter-rotating streamwise vortices, which dominated the wake of the ICE3. The wakes from large roof-angle geometries, which were dominated by large-scale separation, did exhibit high slipstream velocities, however such high velocities occurred directly behind the train. This presents no slipstream risk to a track-side person or infrastructure—obviously the train itself is the safety concern in that area! The streamwise vortices moving downwards and outwards in the low roof-angle cases are what cause the large slipstream values beyond the cross-stream extent of the train.

Investigation of the unsteady wakes from the different tail geometries identified that all wakes exhibited periodic, sinusoidal spanwise oscillations at a frequency of $St_W \approx 0.2$. This is attributed to vortex shedding occurring from the sides of the train. However, the cross-stream oscillations of the wake were significantly wider when this vortex shedding interacts and merges with the streamwise vortices, causing the streamwise structures to oscillate. This wide fluctuation in the wake is the cause of the high standard deviation in the near-wake peak and resulting high peak magnitudes of instantaneous slipstream velocity.

The sensitivity of the slipstream results to the wake structure, in particular, identifying that streamwise vortices interacting with vortex shedding causes the highest slipstream, reinforce the conclusion that the unsteady periodic wake of the ICE3 is the cause of the largest slipstream velocities. Further, the insight from this study provides an opportunity to better optimise a HST's geometry to reduce slipstream risk. Possible avenues for further research would be to examine ways to suppress vortex shedding to reduce the spanwise fluctuations of the wake. Alternatively, reducing the coherence of the streamwise vortices would also reduce peak slipstream velocity. Finally, forcing large-scale separation would reduce slipstream as shown directly in these results, but would also likely increase the pressure drag on the vehicle.

References

[1] C.J. Baker, The flow around high speed trains, J. Wind Eng. Ind. Aerodyn. 98 (2010) 277–298.

[2] C. Baker, A. Quinn, M. Sima, L. Hoefener, R. Licciardello, Full scale measurement and analysis of train slipstreams and wakes: Part 1 ensemble averages, Proc. Inst. Mech. Eng. Part F: J. Rail Rapid Transp. 228 (5) (2012) 451–467.

[3] J.R. Bell, D. Burton, M.C. Thompson, A.H. Herbst, J. Sheridan, Wind tunnel analysis of the slipstream and wake of a high-speed train, J. Wind Eng. Ind. Aerodyn. 134 (2014) 122–138.

[4] J.R. Bell, D. Burton, M.C. Thompson, A.H. Herbst, J. Sheridan, Moving model analysis of the slipstream ad wake of a high-speed train, J. Wind Eng. Ind. Aerodyn. 136 (2015) 127–137.

[5] C.W. Pope, Effective Management of Risk from Slipstream Effects at Trackside and Platforms, Rail Safety and Standards Board – T425 Report, 2007.

[6] ERA, European Rail Agency, EU Technical Specification For Interoperability Relating to the Rolling Stock Sub-System of the Trans-European High-Speed Rail System (HS RST TSI), 2008, 232/EC.

[7] CEN, European Committee for Standardization, Railway Applications – Aerodynamics Part 4: Requirements and Test Procedures for Aerodynamics on Open Track, CEN EN 14067-4, 2009.

[8] M. Weise, M. Schober, A. Orellano, Slipstream velocities induced by trains, Proceedings of the WSEAS International Conference on Fluid Mechanics and Aerodynamics, Elounda, Greece (2006).

[9] T. Muld, G. Efraimsson, D.S. Hennigson, Flow structures around a high-speed train extracted using proper orthogonal decomposition and dynamic mode decomposition, Proc. Inst. Mech. Eng. Part F: J. Rail Rapid Transp. 57 (2012) 87–97.

[10] J.R. Bell, D. Burton, M.C. Thompson, A.H. Herbst, J. Sheridan, Flow topology and unsteady features in the wake of a generic high-speed train, J. Fluids Struct. 61 (2016) 168–183.

[11] J.R. Bell, D. Burton, M.C. Thompson, A.H. Herbst, J. Sheridan, Dynamics of trailing vortices in the wake of a generic high-speed train, J. Fluids Struct. 65 (2016) 238–256.

[12] T. Muld, G. Efraimsson, D.S. Hennigson, Mode decomposition and slipstream velocities in the wake of two high-speed trains, Int. J. Railway Technol. 2 (1) (2013) 1–38.

[13] L. Pii, E. Vanoli, F. Polidoro, S. Gautier, A. Tabbal, A full scale simulation of a high speed train for slipstream prediction, in: Proceedings of the Transport Research Arena, Paris, France, 2014.

[14] H. Hemida, C. Baker, G. Gao, The calculation of train slipstreams using large-eddy simulation, Proc. Inst. Mech. Eng. Part F: J. Rail Rapid Transp. 228 (1) (2014) 25–36.

[15] R.S. Raghunathan, H.D. Kim, T. Setoguchi, Aerodynamics of high-speed railway train, Prog. Aerosp. Sci. 38 (2002) 469–514.

[16] F. Cheli, F. Ripamonti, D. Rochi, G. Tomasini, Aerodynamic behaviour investigation of the new EMUV250 train to cross wind, J. Wind Eng. Ind. Aerodyn. 98 (2010) 189–201.

[17] T. Morel, Effect of base slant on flow in the near wake of an axisymmetric cylinder, Aeronaut. Quart. (1980) 132–147.

[18] S.R. Ahmed, Influence on base slant on the wake structure and drag of road vehicles, J. Fluids Eng. Trans. ASME 105 (4) (1983) 429–434.

[19] V. Ozbolat, T. Tunay, B. Sahin, Effects of rear slant angles on the flow characteristics of ahmed body, Exp. Therm. Fluid Sci. 57 (2014) 165–176.

[20] G. Vino, S. Watkins, P. Mousley, J. Watmuff, S. Prasad, Flow structures in the near-wake of the ahmed model, J. Fluids Struct. 20 (2005) 673–695.

[21] DIN Standards Committee Railway/Normenausschuss Fahrweg und Schienenfahrzeuge (FSF). <www.fsf.din.de>, 2014.

[22] P.W. Bearman, D.D. Beer, E. Hamidy, J.K. Harvey, The Effect of a Moving Floor on Wind-tunnel Simulation of Road Vehicles, SAE Technical Paper No. 880245, 1988.

[23] S. Krajnović, L. Davidson, Influence of floor motions in wind tunnels on the aerodynamics of road vehicles, J. Wind Eng. Ind. Aerodyn. 93 (2005) 677–696.

[24] Xi-feng Liang, Ji-qiang Niu, Dan Zhou, Experimental research on the aerodynamic characteristics of a high-speed train under different turbulence conditions, Exp. Therm. Fluid Sci. 80 (2017) 117–125.

[25] H. Kwon, Y. Park, D. Lee, M. Kim, Wind tunnel experiments on korean high-speed trains using various ground simulation techniques, J. Wind Eng. Ind. Aerodyn. 89 (2001) 1179–1195.

[26] R.V. Westphal, R.D. Mehta, Interaction of an oscillating vortex with a turbulent boundary layer, Exp. Fluids 7 (1989) 405–411.

[27] W.R. Pauley, J.K. Eaton, Experimental study of the development of longitudinal vortex pairs embedded in a turbulent boundary layer, AIAA J. 26 (7) (1988) 816–823.

[28] O. Lödgberg, J.H.M. Fransson, P.H. Alfredsson, Streamwise evolution of longitudinal vortices in a turbulent boundary layer, J. Fluid Mech. 623 (2009).

[29] R.K. Strachan, K. Knowles, N.J. Lawson, The vortex structure behind an agreed reference model in the presence of a moving ground plane, Exp. Fluids 42 (2007) 659–669.

[30] T. Muld, G. Efraimsson, D.S. Hennigson, Wake characteristics of high-speed trains with different lengths, Proc. Inst. Mech. Eng. Part F: J. Rail Rapid Transp. 2013. http://dx.doi.org/10.1177/0954409712473922 (published online).

[31] M. Sterling, C.J. Baker, S.C. Jordan, T. Johnson, A study of the slipstreams of high-speed passenger trains and freight trains, Proc. Inst. Mech. Eng. Part F: J. Rail Rapid Transp. 222 (2008) 177–193.

[32] J.R. Bell, D. Burton, M.C. Thompson, A.H. Herbst, J. Sheridan, The effect of length to height ratio on the wake structure and surface pressure of a high-speed train, in: 19th Australasian Fluid Mechanics Conference (AMFC), Melbourne, Australia, 8–11 December, 2014.

[33] J.D. Hooper, A.R. Musgrove, Reynolds stress, mean velocity, and dynamic static pressure measurement by a four-hole pressure probe, Exp. Therm. Fluid Sci. 15 (1997) 375–383.

[34] H.P.A.H. Irwin, K.R. Cooper, R. Girard, Correction of distortion effects caused by tubing systems in measurements of fluctuating pressures, J. Ind. Aerodyn. 5 (1979) 93–107.

[35] H. Bergh, H. Tijdeman, Theoretical and Experimental Results for the Dynamic Response of Pressure Measuring Systems, National Aero and Astronautical Research Institute, Amsterdam, 1965, 328(Report NLR-TRF).

[36] B.R. Gilhome, J.W. Saunders, J. Sheridan, Time Averaged and Unsteady Near-wake Analysis of Cars, SAE Technical Paper, 01(1040), 2001.